

Influence of Cr and Ni on High-Temperature Corrosion Behavior of Ferritic Ductile Cast Iron in Air and Exhaust Gases

M. Ekström · P. Szakalos · S. Jonsson

Received: 25 May 2012 / Published online: 24 February 2013
© Springer Science+Business Media New York 2013

Abstract Due to an expected temperature increase of the exhaust gases in heavy-duty engines in order to meet future emission regulations, there is a need to develop materials that can operate at higher temperatures. The exhaust manifold in the hot end of the exhaust system is specifically affected since the most common material today, SiMo51, is already operating close to its limits. Accordingly, the effects of Cr and Ni-additions on the high-temperature corrosion resistance of this material in air and exhaust gases were examined. It was found that the addition of 0.5 and 1 wt% Cr improved the oxidation resistance in air at 700 and 800 °C by the formation of an SiO₂ barrier layer as well as a Cr-oxide at the oxide/metal interface. However, no Cr-oxide was detected after exposure to exhaust gases, probably due to a water vapor-assisted evaporation of Cr from the oxide. The addition of 1 wt% Ni resulted in a deteriorated SiO₂ barrier layer and reduced oxidation resistance.

Keywords Ferritic ductile cast iron · Water-assisted evaporation · Exhaust manifold

M. Ekström (✉) · S. Jonsson
Division of Mechanical Metallurgy, Materials Science and Engineering,
Royal Institute of Technology, 100 44 Stockholm, Sweden
e-mail: madeks@kth.se

S. Jonsson
e-mail: jonsson@kth.se

P. Szakalos
Division of Surface and Corrosion Science, Chemical Science and Engineering,
Royal Institute of Technology, 100 44 Stockholm, Sweden
e-mail: szakalos@kth.se

Introduction

In the present work, the effects of Cr and Ni additions on the high-temperature corrosion behavior of a ferritic ductile cast iron, intended for use in exhaust manifolds, have been investigated.

Due to more stringent exhaust emission legislations, the exhaust gas temperatures in heavy-duty engines are expected to increase. In the near future, this requires materials that can operate at higher temperatures, especially in the hot-end of the exhaust system. Today, a Si-alloyed ferritic ductile cast iron, called SiMo51, is used in the turbo manifold. This material is already operating close to its limits and higher exhaust temperatures will therefore push the material beyond the required strength and oxidation resistance for the application. A candidate material for replacement of SiMo51 is an expensive high-Ni ductile cast iron, called Ni-resist D5S. Thus, the aim of an ongoing project is to find cheaper replacements that can operate in temperatures up to 800 °C.

The high-temperature corrosion behavior of SiMo51 and Ni-resist in air and exhaust gases has been studied thoroughly by Tholence and Norell [1–4]. When pure iron oxidizes in air at high temperature, it grows a multi-layered scale of FeO, Fe₃O₄ and Fe₂O₃. The oxide scale that is formed on ductile cast iron is characterized by a sub-layer that grows into the material and a top layer that is formed by outward migration of Fe. When Si is added to the alloy, SiO₂ is formed at the oxide/metal interface, providing a barrier to surface and internal oxidation [5]. Simultaneously, SiO₂ can react with Fe, O and FeO in the sub-scale to form fayalite, Fe₂SiO₄ [6, 7]. Since the sub-layer grows down into the substrate containing carbides and graphite nodules, the microstructure of the cast iron has a great influence on the oxidation behavior.

The oxidation resistance of SiMo51 can be improved by adding elements that contribute to a more protective oxide scale. Early studies [8, 9] have shown improvements of the oxidation resistance of grey cast iron at elevated temperatures with small Cr additions, such as 0.5 wt%. Moreover, Ni has been seen to improve the oxidation behavior of ductile cast iron at room temperature [10]. However, the major effect of Ni in ductile cast iron is improvement of the mechanical properties by solution hardening of the iron matrix [11].

Experimental Procedures

Materials and Sample Preparation

Six different alloys have been investigated in the study. The test matrix consisted of SiMo51 and five different modifications with Cr and Ni. The alloys were cast by a commercial foundry in 40 kg ingots, designed to avoid pore formation in the materials. The chemical composition of each material is given in Table 1.

Test samples were cut from as-cast ingots. Coupons with the size 20 × 20 × 4 mm were prepared for the oxidation test conducted in air. For each oxidation condition, three replicate samples were used. Additionally, screws with the diameter of 9 mm

Table 1 Chemical composition given in wt% (Fe bal.)

Alloy	C	Si	Mn	Cr	Ni	Mo	Mg	Cu
SiMo51	3.17	4.15	0.40	0.10	0.04	0.86	0.05	0.14
0.5Cr	3.28	4.23	0.35	0.52	0.06	0.78	0.05	0.11
1Cr	3.28	4.19	0.36	0.94	0.52	0.86	0.05	0.11
1Ni	3.06	4.19	0.38	0.07	1.29	0.86	0.06	0.15
0.3Cr1Ni	3.19	4.20	0.31	0.33	1.23	0.83	0.05	0.11
0.6Cr1Ni	3.23	4.08	0.30	0.72	1.27	0.78	0.04	0.09

were manufactured for the oxidation test in exhaust gases. The test surfaces of the specimens (top and sides of the coupons and the flat end-surface of the threaded screws) were ground with SiC paper down to a finish of 1,200 grit, ultra sonically cleaned in acetone for 15 min, washed with alcohol and deionized water and then finally dried with lint-free paper.

Test Methods and Sample Characterization

Oxidation tests in ambient air were performed in a chamber furnace (model Naber N60/HR) at 700 and 800 °C with exposure times ranging from 6 up to 330 h. The specimens were placed in the furnace before heating. The time for heating up was 1–1.5 h. The exposure time was calculated from the point when the furnace had reached the pre-set temperature. Specimens were taken out from the oven at different exposure times, which resulted in a temperature drop of 50 °C at every take-out followed by a re-heating stage of 10 min. The experiments were repeated once, resulting in six samples per test condition.

The oxidation tests in exhaust gases were carried out by mounting the screws in an exhaust manifold of a diesel test-engine exposing the ground end to the exhaust gases. The engine was run to produce two test series, one for isothermal exhaust temperatures of 700 up to 740 °C and one for thermal cycling between 240 and 730 °C. The exhaust gas composition is given in Table 2. During the tests, the exhaust gas flow during full load was 1,775 kg/h, which is estimated to a gas velocity of more than 100 m/s.

The oxidation in air was followed by measuring the weight gain per surface unit area of the specimens whereas the oxide thickness was measured in order to follow the oxidation in exhaust gases. After exposure, polished cross sections, mounted in conductive Bakelite, were examined with SEM (Zeis Sigma VP with Gemini field

Table 2 Exhaust gas composition, given in mol%

Exhaust gas composition ^a	O ₂	H ₂ O	CO ₂	CO	NO _x	SO _x (ppm)	HC ^c	N ₂
Diesel fuel ^b	4	4	9	0.01	0.03	0.4	0.004	Bal.

^a Measured at 650 °C during full load (1,900 rpm) with an air-to-fuel ratio of 1.6

^b Containing 10 ppm S and 7 % biodiesel

^c Unburned fuel

emission column), EDS (INCA, Oxford Instruments), and EBSD (Zeiss Supra with Gemini field emission column). Oxide phases were further characterized with XRD (D8, Bruker AXS and Cu $K\alpha$ X-ray with energy dispersive detector, SolX Bruker), directly ran on the oxides. Microstructures of the alloys were examined with optical microscopy (Zeiss Axio). Observations were supported by thermodynamic calculations using Thermo-Calc Software.

Results and Discussion

Examination of Microstructures

The microstructure of SiMo51 was confirmed to consist of graphite nodules and M_6C ($M = Fe, Mo, Si$) carbides distributed in a ferritic matrix. Additions of Cr resulted in increased formation of carbides and pearlite. The carbides were observed to be of two types; M_6C and a Cr-rich carbide. Based on Thermo-Calc calculations and EDX analysis, the Cr-rich carbide was likely to be of the M_7C_3 type. Some of the added Cr was dissolved in the ferritic matrix. As expected, the carbide or pearlite content was not influenced by the addition of Ni. Instead, Ni was dissolved in the ferritic matrix (Fig. 1).

Oxidation Kinetics in Air

In the initial stage of oxidation, rapidly growing Fe-oxides nucleated at matrix/graphite and matrix/carbide interfaces forming oxide islands (see Fig. 2). Between them a slow growing Si-rich oxide was observed. Due to its slower growth, it gradually became overgrown and embedded by the Fe-oxide. At this stage, the

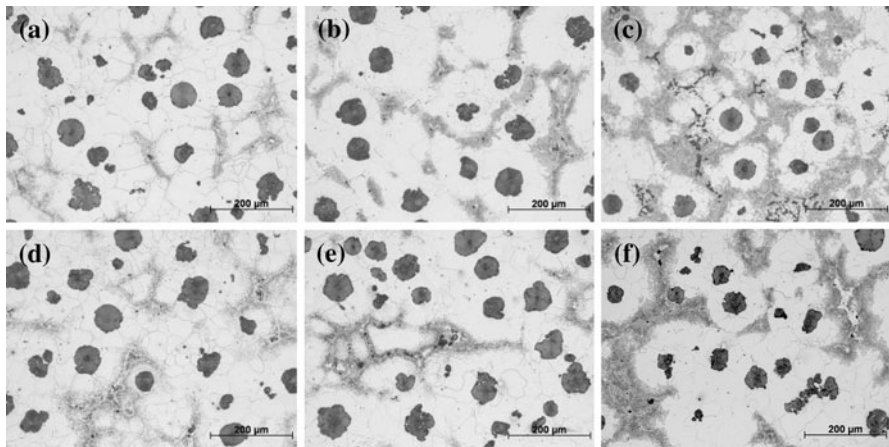


Fig. 1 Micrograph images of **a** SiMo51 with the addition of **b** 0.5Cr, **c** 1Cr, **d** 1Ni, **e** 0.3Cr and 1Ni and **f** 0.6Cr and 1Ni, showing increased carbide and pearlite content as a result of Cr additions

reaction mechanism changed as the Fe-oxide formed a continuous oxide film. The reaction rate then decreased as the oxidation must proceed through solid state diffusion [12]. As the oxide islands grew, the porosity of them increased promoting further oxygen transport into the substrate. The increased porosity may be derived from the fast growth of the oxide but also from the escape of CO/CO₂ gas, which is likely to form when graphite nodules are oxidized. The porosity was observed to be more pronounced at higher temperatures.

In the oxidation test performed in air at 700 °C, an improvement of the oxidation resistance was seen with the addition of both Cr and Ni (see Fig. 3). A higher Cr-content was linked to lower oxidation rate.

In oxidation at 800 °C, the Cr-alloys showed better oxidation resistance compared to the Ni-alloys. Alloying with 0.5Cr proved to be most favorable and was the only alloy that showed a protective oxidation behavior with a stabilized oxide growth. The alloys with Ni-additions showed a catastrophic oxidation behavior with a large weight gain.

Oxidation Kinetics in Exhaust Gases

In the oxidation test conducted in exhaust gases, the effect of Cr and Ni was not as significant as in air.

During the oxidation test conducted under thermal cycling conditions for 700 h, cracks were formed in the outer Fe-oxide scale, probably caused by thermal stresses in the scale due to different thermal expansion coefficients of the alloy and the oxide. The oxide scale thickness of SiMo51, given in Table 3, was in the range of 85–195 μm. The addition of 1Cr showed a slightly lower scale thickness whereas the addition of 1Ni showed similar oxide growth as SiMo51.

In the oxidation test performed under isothermal conditions at temperatures between 700 and 740 °C for 50 h, no significant improvement with Ni or Cr could be observed, see Fig. 4.

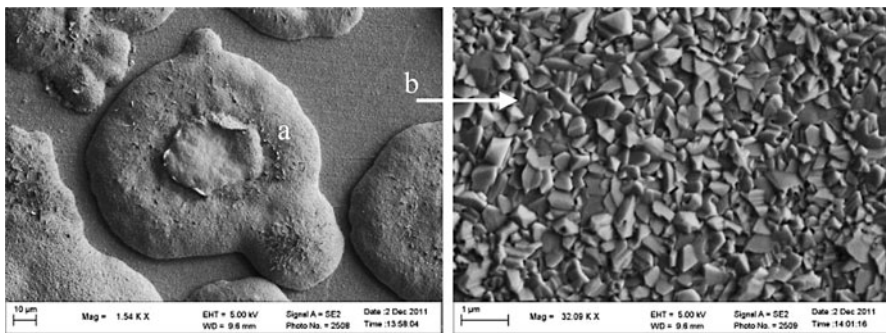


Fig. 2 SEM image of SiMo51 oxidized in air at 800 °C for 96 h. Fe-oxide (a) nucleated at matrix/graphite and matrix/carbide interfaces and grew to oxide islands. A compact layer of Si-rich oxide (b) was formed on the substrate surface and was gradually embedded by the Fe-oxide

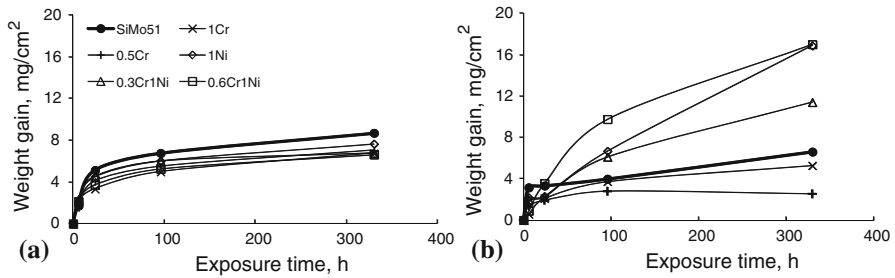
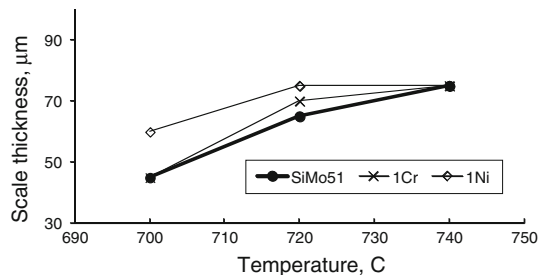


Fig. 3 Weight gain curves after exposure in air at **a** 700 °C and **b** 800 °C. Same symbols in both figures

Table 3 Scale thickness, given in μm , of SiMo51 with additions of 1Cr and 1Ni, respectively, during oxidation in exhaust gases under thermal cycling conditions for 700 h

Alloy	Scale thickness range	Average scale thickness
SiMo51	85–195	140
1Cr	115–135	125
1Ni	115–185	153

Fig. 4 Oxide scale thickness of SiMo51, 1Cr and 1Ni during isothermal exposures in exhaust gases for 50 h



Characterization of Phases in the Oxide Scale

Thermo-Calc Calculations

The influence of Cr and Ni on the oxide scale structure and the microstructure of SiMo51 was examined by thermodynamic equilibrium calculations using Thermo-Calc Software. In the calculation of the oxide scale structure, the TCFE6 and the SSUB4 data bases were used for the matrix and for the oxides, respectively. The fraction of phases as a function of oxygen partial pressure was calculated and plotted. Based on these calculations, Cr is believed to affect the oxide scale by forming a spinel, FeCr_2O_4 and the more protective Cr_2O_3 oxide at exposures in O_2 -atmosphere at 700–800 °C. Furthermore, the addition of Ni was calculated to result in the formation of another spinel, FeNi_2O_4 . Illustrations of the calculated oxide scale structures are shown in Fig. 5. In both of the alloys, the alloying elements, Si, Cr and Ni have been calculated to form oxides in the outer oxide layers.

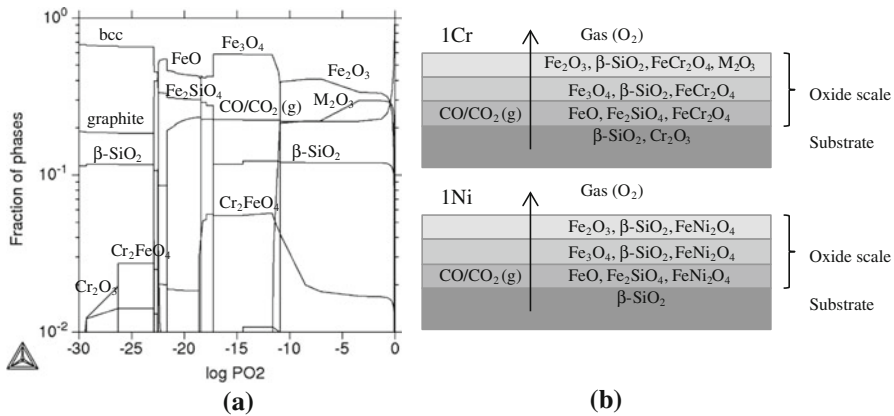


Fig. 5 **a** Amount of phases versus oxygen partial pressure calculated with Thermo-Calc for 1Cr when oxidized in pure oxygen of 700 °C, **b** illustration of oxide scale structures for 1Cr and 1Ni, calculated with Thermo-Calc. The arrows indicate flow of CO/CO₂(g)

However, diffusion properties of the elements are not taken into account, why the authentic oxide scales may differ from the calculated scale structures. Also, β-SiO₂ is the high-temperature form of silica and transforms to α-SiO₂ at lower temperatures.

Calculations of the microstructure, using the TCFE6 database, showed a significant effect on the ferrite to austenite transformation temperature by alloying with Ni. It was noticed, despite the low alloying amount, that Ni lowered this temperature (i.e. the A₁-temperature) by 30 °C. Ni is known as an austenitic promoter [13] whereas Si and Cr shift the A₁-temperature upward and thereby increase the useful temperature range of the ferritic alloy [14]. The phase transformation causes a volume change to occur and is detrimental to the oxidation protection as cracks can be formed in the silica barrier layer [14]. For SiMo51, the starting temperature of the transformation was calculated to occur at 830 °C. The 1Ni addition resulted in a reduction of the starting temperature down to 800 °C. This can be a possible explanation for the deteriorated oxidation resistance at 800 °C for the Ni-containing alloys. The 1Cr alloy contained 0.52 % Ni whereas the 0.5Cr alloy contained only 0.06 % Ni. The higher Ni-content of the former alloy may be the reason for its worse oxidation behavior.

SEM/EDS

From SEM observations of the alloys exposed to air, three distinct oxide layers could be distinguished. The structure of SiMo51 was observed to consist of an outer Fe-oxide (top layer), an inner mixed oxide of Fe and Si (sub-layer) and a thin and compact SiO₂ layer at the oxide/metal interface. The continuous SiO₂ layer was found to be formed from SiO₂ precipitates at the oxide/metal interface, which at later stages, coalesced and formed a compact barrier layer. The sub-layer contained both oxidized and unoxidized graphite nodules as well as carbides, indicating an inward growth of the oxide with the interface of the outer and inner oxide more or

less coinciding with the original substrate surface. The outer oxide was formed by outward diffusion of Fe, which resulted in an inner oxide with high porosity due to Fe depletion.

The addition of Cr resulted in a Cr-oxide at the oxide/metal interface, which, combined with Si forming SiO_2 at the oxide/metal interface as well as being present in the sub-layer, increased the protective properties of the scale. The presence of Cr and Si in the oxide scale is illustrated in the EDS mapping images in Fig. 6. The diffusion of Cr to the oxide/metal interface increased with the temperature and with the time of oxidation. After short exposure times (6 h) no distinct Cr layer could be observed. When alloying with 1Cr, Cr-oxide was detected at both 700 and 800 °C after 24 h of exposure. The alloy containing 0.5Cr formed Cr-oxide only at 800 °C. It was also observed that 0.5Cr had formed a continuous and compact silica layer at 800 °C whereas 1Cr formed an irregular silica layer. Furthermore, SEM observations of the Ni-containing alloys also showed the formation of non continuous SiO_2 layers at 800 °C. Figure 7 shows an irregular silica layer formed on 1Ni. All of the alloys showed a deteriorated oxidation resistance at the higher temperature with no sign of stabilized oxide growth, which can be explained by the absence of a compact SiO_2 barrier layer. Perhaps the breakdown of the SiO_2 layer is linked to the ferrite-to-austenite phase transformation predicted by Thermo-calc. The accompanying volume changes may break the layer. Another explanation may be that the original SiO_2 layer formed on the specimen surface (see Fig. 2) is pushed down and broken up by the growing Fe-oxide nodules. The layer indicated by arrow *e* in Fig. 7a may have been formed in this way. Clearly it is located between the growing Fe-oxide island and the matrix.

The growth of the oxide scale in exhaust gases differed from those in air in the sense that a continuous oxide scale had formed already after short exposure times, such as 7.5 h. The faster oxide growth in exhaust gases can be derived from the high flow rate of the exhausts combined with the presence of oxidative species, such as $\text{H}_2\text{O}(\text{g})$ and $\text{CO}_2(\text{g})$. Moreover, P, Ca and Zn were detected in the outer Fe-oxide scale. This points at the presence of engine oil residues in the exhaust gases carrying these elements. The elements in the oil did not manage to diffuse into the sub-layer, but formed large P-rich precipitates in the top layer.

In the oxidation test conducted under thermal cycling conditions, no Cr was detected neither at the oxide/metal interface nor in the oxide scale. The absence of Cr-oxide can, to some extent, be explained by a water vapor-assisted evaporation of Cr from the oxide. This effect was studied by Asteman et al. [15], who observed Cr evaporation in $\text{O}_2/\text{H}_2\text{O}$ mixtures already at 600 °C in gas flow rates of 5–10 cm/s.

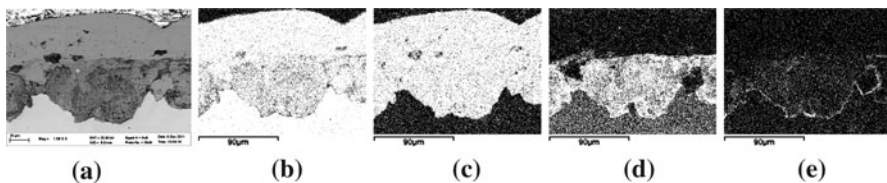


Fig. 6 EDS mapping of 1Cr, exposed to air at 800 °C for 96 h, showing **a** the SEM (BSE) image and the distribution of **b** Fe, **c** O, **d** Si and **e** Cr

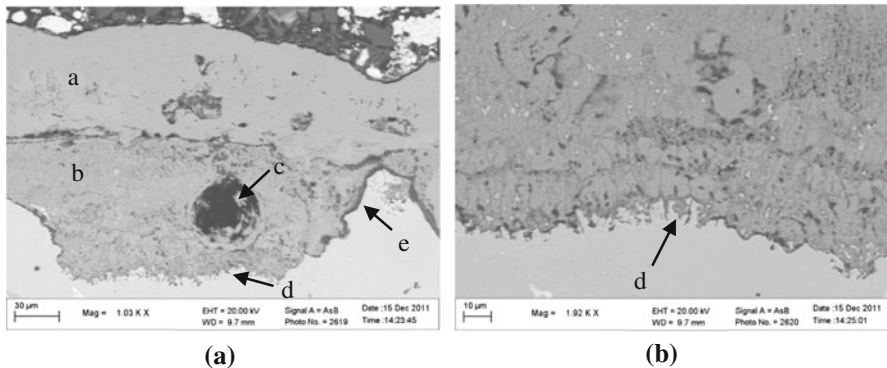


Fig. 7 **a** SEM (BSE) image of oxide scale formed on 1Ni at 800 °C after 96 h of exposure in air, with a scale structure of *a* outer Fe-oxide, *b* inner Fe–Si-oxide with Ni-rich precipitates, *c* partly oxidized graphite nodule, *d* irregular oxide/metal interface with a non uniform SiO₂ layer and *e* compact SiO₂ layer. **b** SEM (BSE) image with the lower region in the left image magnified

Asteman observed an increase in evaporation rate with increasing gas flow rate. Compared to his study, the flow rates in the present study were much higher, promoting the evaporation even further.

On all alloys subjected to thermal cycling, internal oxidation with Si-precipitates was found after 700 h of exposure. This implies that the formation of the healing SiO₂ layer was suppressed. The oxidation test was partly ran at low temperatures, i.e. 240 °C, which may have reduced the Si-diffusion toward the surface. However, all of the alloys did manage to form continuous SiO₂ layers during the thermal cycling conditions.

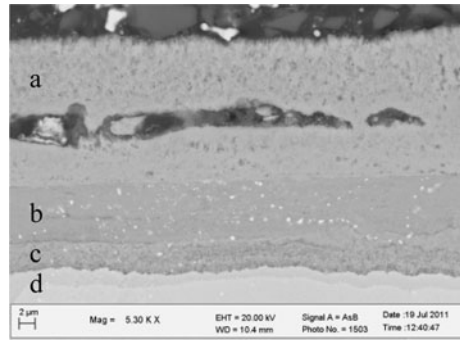
In the isothermal exposures at 700, 720 and 740 °C for 50 h, Cr also failed to form Cr-oxide at the oxide/metal interface or in the oxide scale. The results showed that 1Ni formed thicker oxides compared to SiMo51. This could be derived from the absence of the compact SiO₂ layer. Instead, larger precipitates of SiO₂ distributed in the Fe-oxide were seen at all temperatures. 1Cr also formed SiO₂ precipitates instead of a compact layer at 700 °C, but managed to form a barrier layer at the higher temperatures.

All alloys showed a four layered oxide scale structure, see Fig. 8. The outer Fe-oxide contained P-rich precipitates originating from engine oil and the second layer was a mixed Fe–Si-oxide, similar to the one formed in air. Below, a mixed Fe–Si-oxide with precipitates of carbide forming elements and SiO₂ was present. In 1Ni, Ni-rich precipitates were also found in this layer. SiMo51 formed the most protective oxide scale at the lowest temperature with a continuous SiO₂ layer at the oxide/metal interface. 1Cr and 1Ni only formed larger SiO₂ precipitates distributed in the oxide layer at this temperature. At 720 and 740 °C, 1Cr managed to form a continuous SiO₂ layer while 1Ni only formed isolated precipitates at all temperatures. All of the alloys formed an innermost layer with internal oxidation.

XRD

XRD-analysis of the oxides formed at 800 °C after 96 h of exposure in air, confirmed the presence of Fe₂O₃ (hematite) and Fe₃O₄ (magnetite) in the oxide

Fig. 8 SEM image of oxide scale formed on SiMo51 exposed to exhaust gases of 700 °C for 50 h, showing a scale structure of *a* Fe-oxide with P-rich precipitates, *b* mixed Fe–Si-oxide with precipitates of carbide forming elements, *c* mixed Fe–Si-oxide with SiO₂ precipitates and *d* internal oxidation



scales formed on SiMo51, 1Cr and 1Ni. According to the analyzing software, the reported magnetite may also be a spinel containing Cr or Ni. Neither FeO (wüstite), Fe₂SiO₄ (fayalite) or SiO₂ were detected. Peaks of Fe bcc indicated a total penetration of the X-rays through the scales. In the 0.5Cr-alloy, which showed a superior oxidation resistance at 800 °C compared to SiMo51, only hematite and bcc Fe were detected. The absence of magnetite indicated a reduction of the oxide growth at an early stage.

From the analysis of the samples exposed in exhaust gases, no differences could be revealed from the alloys exposed to air. Hematite and magnetite were identified in all oxide scales.

Electron Backscatter Diffraction (EBSD)

An EBSD analysis was done on all alloys exposed to air of 800 °C for 96 h as well as the samples exposed to exhaust gases during thermal cycling.

Figure 9 shows an EBSD orientation map as well as a phase map of the oxide scale formed on 1Cr exposed in air of 800 °C for 96 h. The dark regions represent areas where diffraction patterns could not be gained either due to imperfections in the surface, such as pores, or to areas where the phase could not be identified. SEM analysis confirmed that most of the dark areas were caused by the high porosity of the oxide scale. From the appearance, the oxide scales formed in air seemed to be more porous than those formed in exhaust gases.

In the top layer, hematite was detected at the oxide/gas interface. A cubic phase with an fcc arrangement was detected underneath this oxide as well as in the areas in the sub-layer where the graphite nodules had been oxidized. According to the results predicted by Thermo-Calc and the results from the XRD analysis, cubic fcc phases likely to be formed are magnetite or the spinel, M₂FeO₄ (M = Cr or Ni). The oxide present underneath the hematite layer as well as the oxidized graphite nodules were presumed to be magnetite, since these areas only contained Fe and O. Fayalite, which possesses an orthorhombic crystal system, was not detected. From EDS results, Si is clearly present in the compact barrier layer at the oxide/metal interface as well as in the sub-scale. This indicates either a presence of amorphous SiO₂ or of a crystalline phase in such small amount that it could not be characterized.

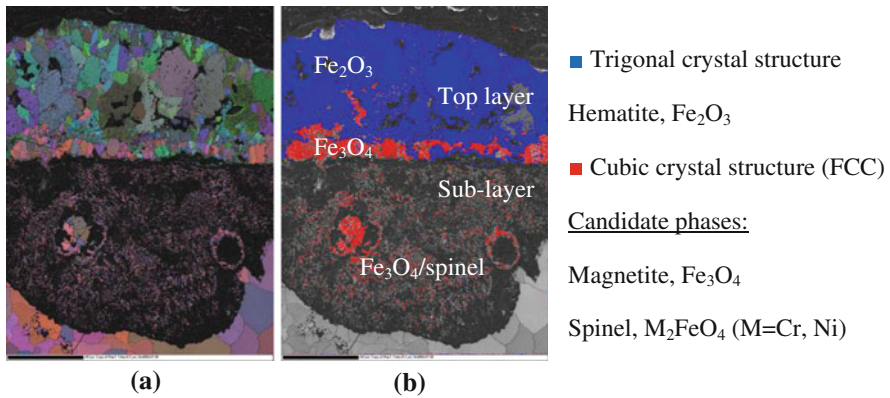


Fig. 9 EBSD orientation map **a** and phase map **b** of 1Cr oxidized in air of 800 °C for 96 h, showing a top layer with large grains of hematite and magnetite and a sub-layer with small grains of magnetite and/or spinel phases

No information of the composition of the phases formed at the oxide/metal interface could be obtained with this method. SEM images confirm a high porosity in this area, which can explain the poor diffraction patterns. Also, since the resolution limit is 10 nm with this method, oxides with smaller grains cannot be detected.

Similar results were observed for all alloys.

In the oxidation in exhaust gases, the hematite layer was observed to be much thinner than the one formed in air, which can be derived from the lower oxygen partial pressure in the exhaust gases.

Conclusions

During exposure to air and exhaust gases, SiMo51 showed a multi-layered oxide scale with layers of hematite and magnetite growing outwards, a sub-scale of magnetite and spinel phases growing into the substrate and a barrier layer of SiO₂ at the oxide/metal interface. Exposure to air resulted in an initial formation of Fe-oxide islands that gradually grew together whereas exposure to exhaust gases resulted in scales covering the metal surface already after a couple of hours.

The SiO₂ formation was found to be slower in exhaust gases. SiMo51 and 1Cr did, however, form a distinct silica layer. The Ni-alloys did not manage to form continuous silica layers in any of the test conditions.

The addition of Cr resulted in improved oxidation resistance in air at both 700 and 800 °C by combination of SiO₂ and a Cr-oxide at the oxide/metal interface. Thermo-Calc suggested the formation of Cr₂O₃ and the spinel, Cr₂FeO₄. Results from XRD analysis pointed at the presence of Cr₂FeO₄ in the oxide scales. The 0.5Cr alloy showed better oxidation resistance than 1Cr at 800 °C, even though the presence of Cr at the oxide/metal interface was lower. It was seen that the former alloy formed a more compact SiO₂ barrier layer, which reduced the oxidation at an

early stage. No Cr-oxide formation was observed during exposure to exhaust gases at the selected temperatures and exposure times. One possible explanation for this is the presence of water vapor-assisted Cr evaporation from the oxide. The effect has been observed to be increased by high gas flow rates.

The addition of Ni caused, according to Thermo-Calc, a reduction of the ferrite to austenite transformation temperature. None of the alloys containing 1Ni managed to form a compact and continuous SiO₂ barrier layer at 800 °C, which lead to a deteriorated oxidation behavior. The volume change caused by the phase transformation, is a possible explanation for the disrupted SiO₂ formation. Another explanation may be that the growing Fe-oxide nodules have pushed the silica layer down and thereby caused its fracture.

Acknowledgments This work was done within The Department of Materials Science and Engineering and the Department of Chemical Science and Engineering at the Royal Institute of Technology, KTH in co-operation with Scania CV AB. The authors acknowledge Vinnova for financial support. The oxidation tests in exhaust gases were performed at Scania CV AB and the authors are grateful to J. Boman for valuable support. The authors also thank Dr. P. Hedström, KTH for running the EBSD-analysis and the technicians at Materials Technology, Scania CV AB for support of sample preparation.

References

1. F. Tholence and M. Norell, *Materials Science Forum* **369–372**, 197 (2001).
2. F. Tholence and M. Norell, *Surface and Interface Analysis* **34**, 535 (2002).
3. F. Tholence and M. Norell, *Journal of Physics and Chemistry of Solids* **66**, 430 (2005).
4. F. Tholence and M. Norell, *Oxidation of Metals* **69**, 13 (2008).
5. W. Fairhurst and K. Röhrig, *Foundry Trade Journal* **146**, 657 (1979).
6. A. Reynaud, *Corrosion of Cast Irons*, (Elsevier, Sévred Cedex, 2010), p. 1741.
7. R. C. Logani and W. W. Smeltzert, *Oxidation of Metals* **3**, 15 (1971).
8. C. O. Burgess, *Proceedings of the American Society for Testing Materials* **39**, 604 (1939).
9. C. O. Burgess and A. E. Shrubbsall, *AFA Transactions* **50**, 405 (1942).
10. Kent, K. Randy, US 4702886 Corrosion resistant Ni alloys ductile cast irons of ferrite structure Romac Industries Inc., Seattle, Wash 1987-10-27.
11. C. Labrecque and M. Gagné, *Canadian Metallurgical Quarterly* **37**, 343 (1998).
12. P. Kofstad, *High Temperature Corrosion*, (Elsevier Applied Science Publishers Ltd., London, 1988), p. 142.
13. J. R. Davis, *ASM Specialty Handbook—Heat Resistant Materials*, (ASM International, Materials Park, 1977), p. 3.
14. K. Röhrig, *VDI Z* **5**, 27 (1985).
15. H. Asteman, J. E. Svensson and L. G. Johansson, *Corrosion Science* **44**, 2635 (2002).